Monthly Notices
of the
ROYAL ASTRONOMICAL SOCIETY

MNRAS **437,** 606–621 (2014) doi:10.1093/mnras/stt1942
Advance Access publication 2013 November 11

Herschel, *Spitzer* and Magellan infrared observations of the star-forming region RCW 121 (IRAS 17149−3916)⋆

M. Tapia,[1]† P. Persi,[2] M. Roth,[3] D. Elia,[2] S. Molinari,[2] H. P. Saldaño[4] and M. Gómez[4]

[1]*Instituto de Astronomía, Universidad Nacional Autónoma de México, Apdo. Postal 877, 22830 Ensenada, BC, Mexico*
[2]*INAF – Istituto Astrofisica e Planetologia Spaziale, Via Fosso del Cavaliere 100, I-00133 Roma, Italy*
[3]*Las Campanas Observatory, Carnegie Institution of Washington, Casilla 601, La Serena, Chile*
[4]*Observatorio Astronómico de Córdoba, X5000BGR Córdoba, Argentina*

Accepted 2013 October 5. Received 2013 October 5; in original form 2013 September 3

ABSTRACT

We present new deep near-infrared broad- and narrow-band imaging and low-resolution spectroscopy of the star formation region RCW 121 (IRAS 17149−3916) which we analyse in combination with *Herschel* (70, 160, 250, 350 and 500 μm) and *Spitzer* (3.6, 4.5, 5.8 and 8 μm) images. The near-infrared photometry reveals the presence of a stellar cluster of approximate size of 92 arcsec which is composed of at least 264 members, approximately 25 per cent of these showing excess emission at $\lambda > 2.0\,\mu$m, indicative of circumstellar discs. Isochrones corresponding to ages 0.5–1.0 Myr and $A_V = 7.8$ fit well the position of a large fraction of likely cluster members in the K_s versus $H - K_s$ diagram. We find three massive star-forming cores located in the boundaries of an expanding H II region ionized by a central O-type star. From their far-infrared spectral energy distributions (SEDs) we derive masses and temperatures of the dense cores. When these young stellar objects (YSOs) have warm emission components, the 1.2–500 μm SEDs are fitted with Robitaille et al.'s star–disc-envelope model to obtain their physical parameters. The masses of the three YSOs are between 8 and 10 $M_\odot$. The youngest site (core I) is undetected at $\lambda < 100\,\mu$m and is at the earliest evolutionary stage that can currently be detected. The other two cores (II and III) contain YSOs of similar masses and have near-infrared counterparts, which imply a more advanced evolutionary stage. The YSO at core II has been found to have associated a jet, with strong H_2 line emission, co-existing with an H_2O maser source. RCW 121 is another example of multiple star formation being triggered by the expansion of a single H II region.

Key words: circumstellar matter – stars: formation – infrared: ISM.

1 INTRODUCTION

The idea that an H II region is capable of triggering the formation of new generation of stars, either by compressing neutral material as it expands into its surroundings or by creating a shock front into pre-existing dense dust clumps or obstacles (Elmegreen 1998 and references therein), has recently received ample observational support. A considerable number of expanding ionized 'bubbles' have been found to harbour active star-forming regions along their borders (e.g. Anderson et al. 2012 and references therein). Similarly, many bright-rimmed photodissociation regions (PDRs) in the vicinity of O-stars (and their associated H II regions) have also been found to contain extremely young stellar objects (YSOs) inside (e.g. Tapia et al. 2006). Detailed observational studies of places where these kind of conditions are suspected (like RCW 121) should provide important information for understanding when and how these triggered star formation processes occur.

Originally discovered by Haro (1952) as a diffuse, round, Hα nebulosity (Haro 3−6), RCW 121 [$(l, b) = (348.^\circ24, 0.^\circ98)$] is now known to be a complex star-forming region. It is listed in the catalogue of Hα-emission regions in the Southern Milky Way (RCW: Rodgers, Campbell & Whiteoak 1960). Radio continuum observations at several wavelengths (Wright et al. 1994; Arnal, Duronea & Testori 2008) indicate that the H II region has a size of 2.7×2.3 arcmin^2 at 4.85 GHz. Very recently Sánchez-Monge et al. (2013) have measured the H II region at 18.0 GHz (2 cm) and 22.8 GHz (1.3 cm). They calculated an ionized gas mass of 2.17 $M_\odot$ and ionizing energy flux of equivalent to one O8.5 zero-age

⋆Based on observations made with the BAADE telescope located at Las Campanas Observatory, CIW, and uses data from the *Spitzer Space Telescope* archive. *Herschel* is an ESA space observatory with science instruments provided by European-led Principal Investigator consortia and with important participation from NASA.

† E-mail: mt@astrosen.unam.mx

main-sequence (ZAMS) star ($L_{\rm Ly} = 1.3 \times 10^{48}\,{\rm s}^{-1}$). A water maser source at 22.235 GHz was also found by these authors to be associated with the region, at $\alpha(2000) = 17^{\rm h}18^{\rm m}23\overset{\rm s}{.}47$, $\delta(2000) = -39^\circ18'40\overset{''}{.}3$.

The source IRAS 17149−3916 was readily identified as the infrared (IR) counterpart of RCW 121, which displays bright CS ($J = 2$–1) line emission (Bronfman, Nyman & May 1996). The presence of a possibly variable 6.7 GHz methanol maser detected by Walsh et al. (1997, 1998) suggests that RCW 121 is a high-mass star-forming region. Using the Swedish–ESO Submillimetre Telescope (SEST), Beltrán et al. (2006) found four massive dust clumps at 1.2 mm which were indicative of internally heated dense cores.

From visual inspection of Two Micron All Sky Survey (2MASS) images, Dutra et al. (2003) found an IR cluster of stars in the direction of RCW 121. The presence of a young cluster of massive stars embedded in the H II region coincident with IRAS 17149−3916 was confirmed by Roman-Lopes & Abraham (2006). By means of $JHK_{\rm C1}$ photometry with a 60-cm telescope and mean seeing of 2 arcsec, these authors listed almost a hundred cluster member candidates brighter than $K_{\rm C1} \simeq 13.8$ in an area of about 1.5×2.0 arcmin^2, 30 per cent of them showing excess emission in the near-IR.

Most of the ionization of this roundish H II region is provided by the bright, visible star 2MASS 17182545−3919086, also named IRS-1 by Roman-Lopes & Abraham (2006) and IRAS 17149−3916nr895 by Bik et al. (2005), located close to the centre of the nebula. Based on its near-IR spectrum, Bik et al. (2005) classified this star as O5-6V. Hereafter, this star will be referred to as central ionizing star. From radial velocities of the methanol maser emission, kinematic distances to the complex ($d_{\rm near}$ and $d_{\rm far}$) of 1.9 and 17.7 kpc were derived by Walsh et al. (1997), while Sewilo et al. (2004) report 2.2 to 14.5 kpc, from the H110α hydrogen emission line and from the H_2CO absorption line, respectively. Throughout this work, we adopt a newly derived value for the distance of 2.0 kpc to the complex, as will be described in the text.

In order to study in more detail this complex high-mass star-forming region, we obtained new subarcsec resolution near-IR broad- and narrow-band images centred on the *IRAS* source. In addition, near-IR spectra in selected positions of the region have also been gathered. These observations are compared with far-IR images from the *Herschel* Infrared Galactic Plane Survey (HI-GAL; Molinari et al. 2010) supplemented with *Spitzer* Galactic Legacy Infrared Midplane Survey Extraordinaire (GLIMPSE) archive images taken with the Infrared Array Camera (IRAC). All observations are described in Section 2. In Sections 3 and 4, we describe the properties of the H II region and associated IR cluster as derived from the multifrequency images. Using far-IR flux densities from *Herschel* images and millimetre data from Beltrán et al. (2006), masses and temperatures are derived for three dense cores in Section 5. In Section 6, their spectral energy distributions (SEDs) obtained by combining near-IR, *Spitzer* and *Herschel* data were fitted with a radiation transfer model including envelope+disc (Robitaille et al. 2006). Finally, Section 7 lists our conclusions.

2 OBSERVATIONS

2.1 Near-infrared images

Near-IR images through standard broad-band $JHK_{\rm s}$ as well as through narrow-band H_2 ($\lambda_0 = 2.125\,\mu$m, $\Delta\lambda = 0.024\,\mu$m) and $Br\,\gamma$ ($\lambda_0 = 2.165\,\mu$m, $\Delta\lambda = 0.022\,\mu$m) filters were collected on the night of 2009 June 11 and 12 using the Perssons Auxiliary Nasmyth Infrared Camera (PANIC) attached to the Magellan Baade 6.5-m telescope at Las Campanas Observatory (Chile). PANIC uses a Hawaii 1024 × 1024 HgCdTe array that provides a 120×120 arcsec^2 field of view with a scale of $0\overset{''}{.}125$ pixel^{-1} (Martini et al. 2004). We obtained nine dithered frames, each of 60, 40 and 20 s integration in J, H and $K_{\rm s}$, respectively, and 60 s in the narrow-band filters offsetting the telescope by 6 arcsec between consecutive exposures. The basic image reduction was performed using the PANIC pipeline (http://code.obs.carnegiescience.edu/panic) which corrects for detector and camera irregularities, produces accurate sky and flat-field images by iteratively combining the observed frames through filtering remnant sources during each iteration and performs the usual corrections to obtain the final reduced images. The measured full width at half-maximum (FWHM) of the point spread function (PSF) was ≃0.7 arcsec and the total useful area covered in the five filters is 123×123 arcsec^2. PSF-fitting photometry was performed using the DAOPHOT stellar photometry package (Stetson 1987) within the Image Reduction and Analysis Facility (IRAF) environment.[1] The photometry was calibrated using several standard stars each night from the extended list of Persson et al. (1998), which includes fainter standards for use with the Magellan telescopes (http://www.lco.cl/telescopes-information/magellan/instruments/panic/panic-online-documentation/panic-manual/new-ir-standards-for-panic/).

A total of 1502 sources were measured in J, H and $K_{\rm s}$, with a further 102 sources measured only in H and $K_{\rm s}$. Nevertheless, in order to avoid contamination of potentially spurious data, only photometric measurements with intrinsic errors smaller than 0.09 and sources brighter than $J = 19.5$ were consider for analysis. All PANIC sources brighter than $K_{\rm s} = 12.5$ were also discarded, as these were approaching the non-linearity regime of the detector. The working PANIC data set included 979 sources with $J\,H\,K_{\rm s}$ and 1516 with reliable data in H and $K_{\rm s}$ only. 29 sources brighter than 12.5 in $K_{\rm s}$ from the 2MASS Point Source Catalogue (Skrutskie et al. 2006) in the area under study were also added, yielding a final data set with 1545 sources with H, and $K_{\rm s}$ reliable measurements, of which 1008 also had good J values. From the photometric error distribution, we estimated 90 per cent completeness limits to be $H = 19.5$ and $K_{\rm s} = 18.2$. At J, this occurs at a fainter magnitude but, for the sake of clarity, only sources with $J \leq 19.5$ were considered for this analysis. The table listing all the individual $J\,H\,K_{\rm s}$ photometry is only available electronically through CDS.[2]

Only 34 unsaturated stars were common to the photometric study of the brightest sources in this region by Roman-Lopes & Abraham (2006), and the comparison yielded $\langle\Delta(J_{\rm PANIC} - J_{\rm RL})\rangle = +0.12$, $\langle\Delta(J-H)_{\rm PANIC} - (J-H)_{\rm RL}\rangle = -0.02$ and $\langle\Delta(H-K_{\rm s})_{\rm PANIC} - (H-K_{\rm C1})_{\rm RL}\rangle = -0.08$, with standard deviations of 0.17, 0.18 and 0.18, respectively. Note that the central wavelength of the $K_{\rm C1}$ filter (2.14 μm) used in Roman-Lopes & Abraham (2006) differs from our PANIC $K_{\rm s}$ filter (2.16 μm).

Fig. 1 shows two three-colour images obtained with PANIC; both are centred close to the nominal *IRAS* source position. The left-hand panel illustrates an image constructed by combining the J (blue), H (green) and $K_{\rm s}$ (red) individual images of the region RCW 121. This $JHK_{\rm s}$ composite image is characterized by a large number of very red sources, confirming the presence of a young stellar cluster.

[1] IRAF is distributed by the National Optical Astronomy Observatory, which is operated by the Association of Universities for Research in Astronomy, Inc. under contract to the National Science Foundation.
[2] http://cdsarc.u-strasbg.fr/viz-bin/qcat?J/MNRAS/

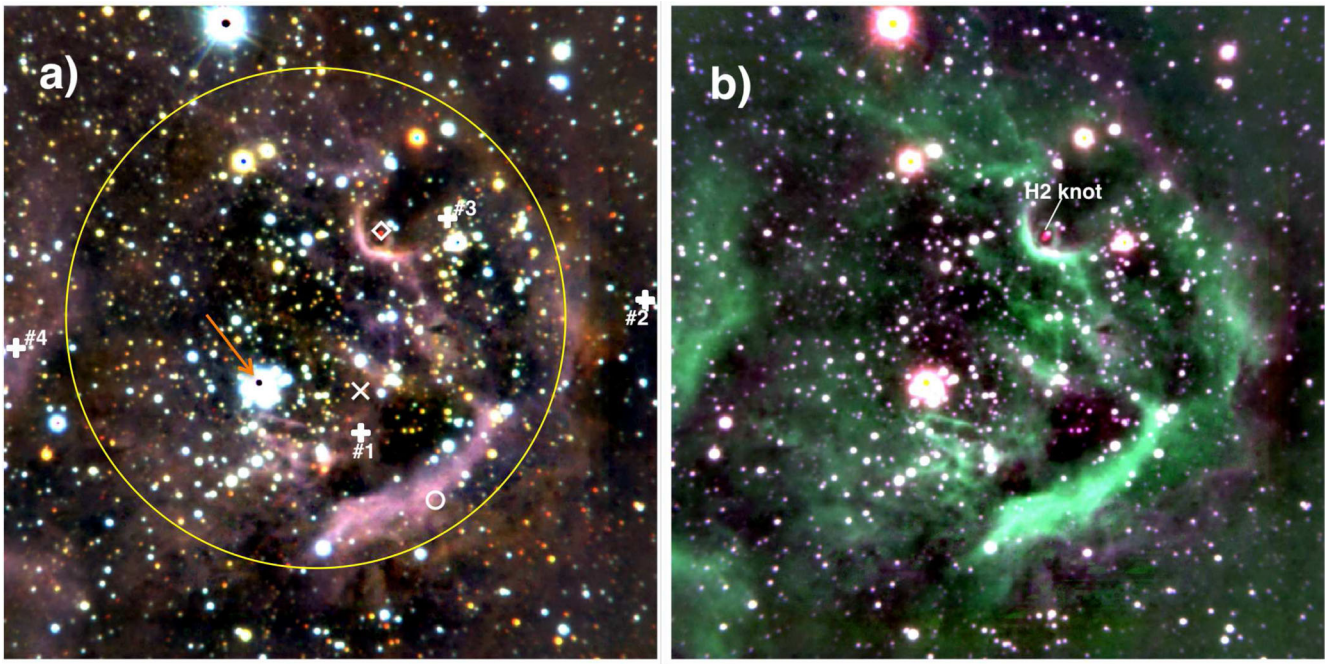

Figure 1. (a) JHK_s three-colour image of RCW 121. The cross (x) indicates the nominal position of IRAS 17149−3916. The small open circle marks the position of the observed 18 GHz continuum emission peak, while the diamond represents the position of the water maser source (Sánchez-Monge et al. 2013). The four 1.2 mm emission peaks, indicating the location of dense cores, from Beltrán et al. (2006), are marked with (+) signs and labelled #1, #2, #3 and #4. The large yellow circle marks the extent of the near-IR cluster (see Section 4) and the orange arrow points to the position of the bright central ionizing O star. (b) Three-colour image made with from the K_s (blue), the Br γ (green) and the H_2 (red) individual frames showing the extended regions where the emission is dominated by the 2.0–2.4 μm continuum, the ionized hydrogen and molecular hydrogen lines, respectively. All intensity scales are linear. Both images are centred at $\alpha(2000) = 17^h18^m24\overset{s}{.}3$, $\delta(2000) = -39°18'59''$ and have an area of 121 × 121 arcsec^2. North is at the top and east to the left.

The basic properties of such IR cluster will be determined in Section 4 by analysing the JHK_s photometric data. The image in the right-hand panel was constructed by combining the K_s (blue), the Br γ (green) and the H_2 (red) individual images such that the regions where Br γ emission dominates appear green, those where the molecular hydrogen line emission dominates are seen red and the extended regions dominated by 2.0–2.5 continuum appear blue. It is apparent that the bright, extended emission in the Br γ line coincides with the extended emission features on the J, H and K_s images, indicating that continuum radiation is scattered by dust particles that are well mixed with the ionized hydrogen. In addition, a conspicuous knot of H_2 emission is located at $\alpha(2000) = 17^h18^m23\overset{s}{.}52$, $\delta(2000) = -39°18'41\overset{''}{.}4$.

2.2 Near-infrared spectroscopy

Low-resolution long-slit spectroscopy was performed on 2012 May 30 with the Folded-port Infrared Echellette Spectropraph (FIRE) mounted on Las Campanas Observatory's 6.5-m Magellan/Baade telescope in its high throughput prism mode. This configuration provides simultaneous spectra from 0.82 to 2.51 μm with spectral resolutions $R_J = 500$, $R_H = 450$ and $R_K = 300$ in the J, H, K_s atmospheric windows. The instrument is described in detail by Simcoe et al. (2013). The fixed slit length is 50 arcsec and its width was set to 0.8 arcsec, which is larger than the typical seeing encountered during our run. The spatial scale is 0.15 arcsec pixel^{-1}. The slit locations and orientations were selected to include the sources with the most extreme red near- and mid-IR colour indices, i.e. the YSO candidates, and also regions where the narrow-band images indicate strong line emission associated with those sources. The slit placings are marked A, B and C in Fig. 2 over a K_s-band grey-scale image. The sources whose spectra were extracted and calibrated are listed in Table 1 with their JHK_s photometry and positions, which are also indicated in Fig. 2. The total on-chip integration time was always 300 s. Contemporaneously we gathered spectra of nearby (or at least with similar airmasses) A0V stars for telluric absorption correction, as well as Ne–Ar comparison lamp frames for wavelength calibration.

The spectra were reduced for wavelength calibration, sky-subtraction, extraction, combination of individual spectra, correction for telluric absorption and flux calibration, using the standard FIRE pipeline reduction described in http://web.mit.edu/~rsimcoe/www/FIRE/ob_data.htm. Final filtering for spurious spikes, selected extraction and flux measurements (with Gaussian fitting) was performed with IRAF's ONEDSPEC package. We extracted spectra of a total of 11 compact sources on the three slits, and only seven of these show emission lines. Figs 3 and 4 show the 1–2.5 μm spectra of the sources with emission lines, while in Tables 2 and 3 the identifications of the emission lines with their measured intensities are reported.

2.3 *Herschel* Infrared Galactic Plane Survey images

RCW 121 (IRAS 17149−3916) was observed in the far-IR within HI-GAL (Molinari et al. 2010), a *Herschel* open time key project aiming at mapping the Galactic plane with the Photodetector Array Camera and Spectrometer (PACS, 70 and 160 μm; Poglitsch et al. 2010) and Spectral and Photometric Imaging Receiver (SPIRE, 250, 350 and 500 μm; Griffin et al. 2010) photometers on board the *Herschel* satellite (Pilbratt et al. 2010). The HI-GAL observations

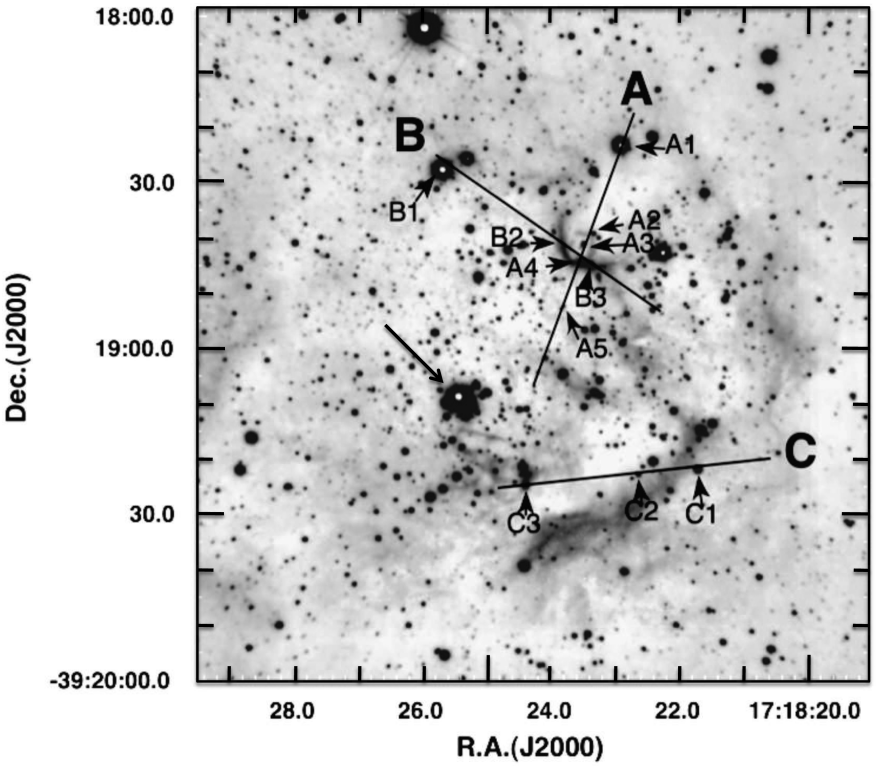

Figure 2. K_s-band image of RCW 121 showing the three slit positions (labelled A, B and C) and the location of the sources whose spectra were extracted. The long arrow marks the position of the central ionizing star.

Table 1. Coordinates and near-IR 1 arcsec aperture photometry of sources for which near-IR spectra are presented.

Position	α(2000) (^{h} ^{m} ^{s})	δ(2000) ($^{\circ}$ $'$ $''$)	J (mag)	H (mag)	K_s (mag)	Notes
IRAS 17149-II						
A2	17 18 23.45	−39 18 39.3	–	–	–	Neb. with star
B3	17 18 23.37	−39 18 44.4	–	15.10 0.03	13.75 0.03	Star in neb.
A3	17 18 23.47	−39 18 40.5	–	18.00 0.10	14.71 0.04	YSO II with jet
A4	17 18 23.51	−39 18 44.6	15.69 0.02	15.04 0.03	13.65 0.03	Neb.
A5	17 18 23.81	−39 18 52.2	16.87 0.01	16.28 0.01	15.95 0.02	Star in neb.
B2	17 18 23.81	−39 18 41.7	15.76 0.02	15.23 0.02	14.00 0.02	Neb.
IRAS 17149-III						
C3	17 18 24.40	−39 19 24.6	17.82 0.05	15.53 0.03	12.80 0.01	YSO III

are arranged in images of $\sim$2.3° $\times$ 2.3° taken at each of the five wavelengths. Our target, in particular, lies in the HI-GAL field centred at $l \simeq 347.^{\circ}5, b \simeq 0.^{\circ}0$, observed by *Herschel* on 2010 September 6 and 7 in SPIRE+PACS parallel mode at a scan speed of 60 arcsec s^{-1}. The data were reduced using the HI-GAL standard pipeline (Traficante et al. 2011).

The maps have pixel sizes 3.2, 4.5, 6, 8 and 11.5 arcsec at 70, 160, 250, 350, 500 μm, respectively. The astrometry on the maps were checked by comparing the positions of several isolated compact sources appearing in both the 70-μm map and in the MIPSGAL survey (Carey et al. 2009). From the images, we performed the source extraction and photometry using the Curvature Threshold Extractor package (CUTEX; Molinari et al. 2011). The upper panel of Fig. 5 shows a three-colour image composed from the 70 μm (blue), 160 μm (green) and 350 μm (red) frames. The three brightest far-IR sources are named IRAS 17149-I, II and III, and their fluxes are reported in Table 4. Source I is unresolved and located at the western border of our 2.2-μm image, while source II appears unresolved on our images (FWHM = 18 arcsec at 250 μm) and, being at precisely the same location, is most probably associated with the H_2O maser and a very red compact near- and mid-IR source with what appears like an H_2 jet emanating from it (see Fig. 1). Finally, source III appears extended (FWHM = 29.6 arcsec at 250 μm) and, in projection, it is closer to the central ionizing O star. The positions of these peaks were further refined by registering the coordinates of the two bright far-IR sources II and III to those of their IRAC counterparts.

2.4 *Spitzer* GLIMPSE archive images

Flux-calibrated images of the IRAS 17149−3916 region from the GLIMPSE (Benjamin et al. 2003; Churchwell et al. 2009) key program survey taken at 3.6, 4.5, 5.8 and 8 μm with IRAC (Fazio et al. 2004) on board the *Spitzer Space Telescope* (Werner et al. 2004) were retrieved from the image archive. The flux densities of the

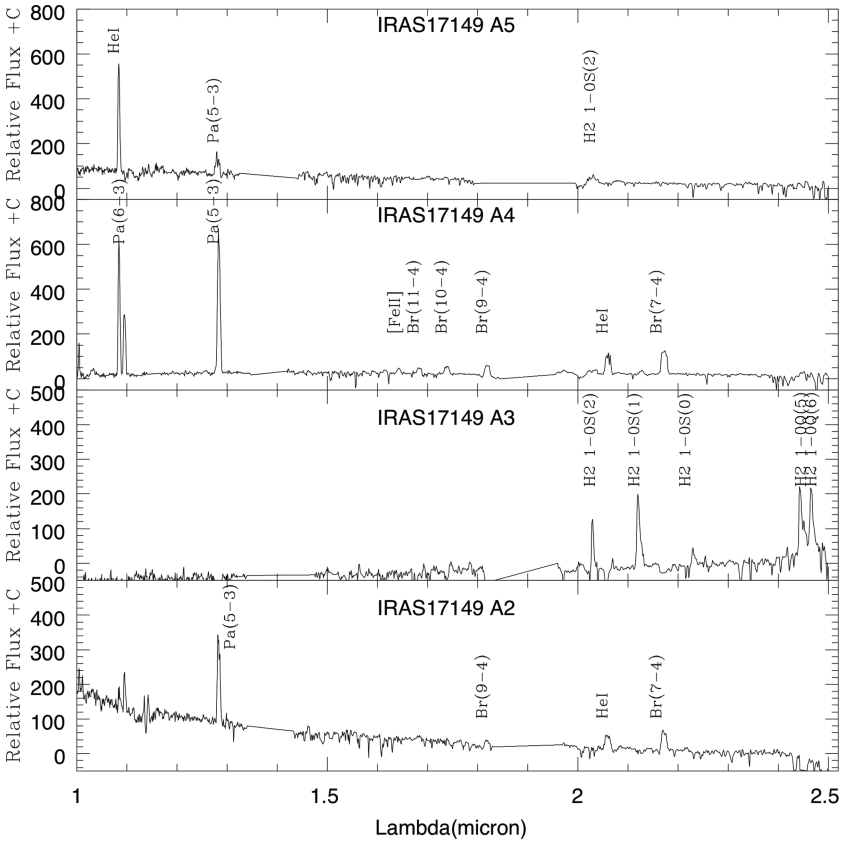

Figure 3. 1.0–2.5 μm spectra of the sources with emission lines along the slit position A.

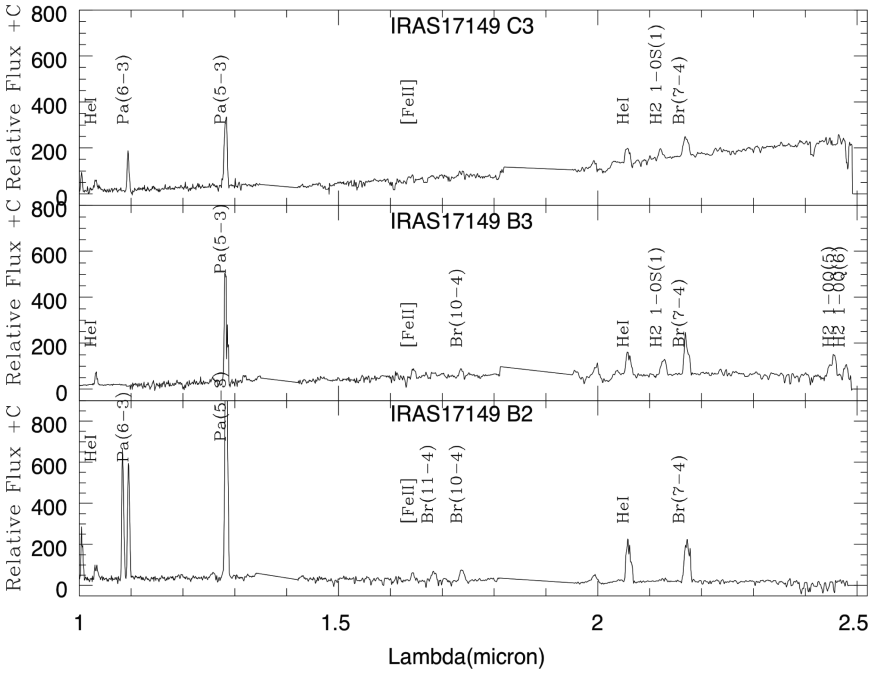

Figure 4. 1–2.5 μm spectra of the sources with emission lines along the slit positions B and C.

mid-IR counterparts of the *Herschel* sources II and III were extracted from the GLIMPSE catalogue. The lower panel of Fig. 5 shows the three-colour 3.6 μm (blue), 4.5 μm (green) and 8 μm (red) image with 70 and 250 μm emission contours from *Herschel* superimposed. Aperture (6 arcsec) photometry was performed of the unresolved sources on the calibrated images with DAOPHOT. The sky value for each source was measured on a ring of radius 4 arcsec and width 1.3 arcsec after filtering for source contamination. A total of 37 point sources could be measured photometrically in the IRAC channel 1 and channel 2 frames. Half of them were identified in

Table 2. Identification and measurement of fluxes and equivalent widths (EWs) of lines in selected spectra extracted from the spectra in slit position A.

Identification	λ (μm)	λ(fit) (μm)	Flux (10^{-18} erg cm^{-2} s^{-1})	EW (Å)
IRAS 17149 A2				
Pa (5–3)	1.283	1.282	2.95	−1.48
Br (9–4)	1.819	1.818	0.81	
He	2.0597	2.0587	1.11	
Br γ	2.171	2.166	0.96	
IRAS 17149 A3				
H2 1–0 S(3)	1.9527	1.9576	0.49	
H2 1–0 S(2)	2.0293	2.0338	0.75	
H2 1–0 S(1)	2.1206	2.1218	1.35	−0.234
H2 1–0 S(0)	2.2302	2.2235	0.23	−0.229
H2 1–0 Q(5)	2.4438	2.4548	0.74	−0.01
H2 1–0 Q(6)	2.4661	2.4750	0.87	−0.013
IRAS 17149 A4				
Pa (7–3)	1.0045	1.0050	0.69	−0.02
He I	1.0328	1.0314	0.79	
He I	1.0843	1,0832	6.10	
Pa (6.3)	1.0950	1.0940	4.02	
Pa (5–3)	1.2833	1.2820	9.30	
Br (11–4)	1.6834	1.6810	0.68	−0.019
Br (10–4)	1.7389	1.7370	0.96	−0-031
Br (9–4)	1.8194	1.8180	1.59	
He I	2.0603	2.0587	5.03	
Br γ	2.1722	2.1660	4.58	
IRAS 17149 A5				
He I	1.0838	1.0832	2.68	−0.10
Pa (5–3)	1.2808	0.2820	1.94	−0.382
H2 1–0 S(2)	2.0300	2.0338	0.73	−0.041

Table 3. Identification and measurement of fluxes and EWs of lines in selected spectra extracted in slit positions B and C.

Identification	λ (μm)	λ(fit) (μm)	Flux (10^{-18} erg cm^{-2} s^{-1})	EW (Å)
IRAS 17149 B2				
Pa (7–3)	1.0050	1.0050	1.13	−0.064
He I	1.0327	1.0314	0.64	−0.027
He I	1.0837	1.0832	3.28	
Pa (6–3)	1.0950	1.0940	2.86	
Pa (5–3)	1.2833	1.2820	10.30	
Br (11–4)	1.6835	1.6810	1.04	
Br (10–4)	1.7383	1.7370	0.77	−0.06
He I	2.0591	2.0587	3.89	
Br γ	2.1725	2.1660	5.14	
IRAS 17149 B3				
He I	1.0322	1.0314	0.26	−0.012
Pa (5–3)	1.2814	1.2822	1.97	−0.018
He II	1.3186	1.3150	0.30	−0.012
Br (10–4)	1.7364	1.7370	0.31	−0.006
H2 1–0 S(2)	2.0376	2.0338	0.89	−0.028
He I	2.0590	2.0587	1.52	−0.037
H2 1–0 S(1)	2.1270	2.1218	1.08	−0.022
Br γ	2.1700	2.1660	1.38	−0.019
H2 1–0 Q(5)	2.4544	2,4548	1.39	−0.029
H2 1–0 Q(6)	2.4786	2.4756	1.60	
IRAS 17149 C3				
Pa (7–3)	1.0045	1.0050	0.37	−0.087
He I	1.0315	1.0314	0.35	−0.027
Pa (6–3)	1.0941	1.0940	0.78	−0.059
Pa (5–3)	1.2825	1.2820	2.62	−0.348
He I	2.0575	2.0587	1.37	−0.013
H2 1–0 S(1)	2.1209	2.1218	0.37	−0.002
Br γ	2.1700	2.1660	1.33	−0.009

2MASS ($K_s < 12.5$) and the other half in our PANIC data sets. The position and photometry of these sources in the 1.2–4.5 μm range are given in Table 5, which also includes relevant notes to each entry. Note that the IRAC images are much shallower than those from PANIC, thus the rather small number of mid-IR counterparts.

3 THE DEVELOPED H II REGION RCW 121 AND ITS DISTANCE

The present Br γ map (see Fig. 1b) delineates the spatial projected structure of the H II RCW 121 with the highest resolution to date. As expected, its appearance on this image is consistent with the considerably lower resolution morphology reported at two radio-continuum frequencies (18.0 and 22.8 GHz) by Sánchez-Monge et al. (2013). As seen on the present images, the H II region appears filamentary, probably caused by inhomogeneous dust clouds within the nebula, but the overall structure is round, probably spherical, with a mean radius of around 40 arcsec, having the star 2MASS 17182545−3919086 very close to its centre. On the Red Digital Sky Survey (DSS2) image, it appears roughly similar, and because of the much lower spatial resolution, the visible emission looks rather homogeneous. Because of this, initially this Hα nebulosity was erroneously classified as a planetary nebula. The energetics of the H II region strongly suggest that the H II region is solely, or mostly, ionized by the abundant ultraviolet (UV) radiation from an O-type central star as has been determined by Sánchez-Monge et al. (2013) and Roman-Lopes & Abraham (2006). The latter authors derived an approximate value of the visual extinction towards the H II region of $A_V = 5.5$ by comparing the integrated $Br\gamma$ line flux with that of the radio-continuum 4.85 GHz emission.

Bik et al. (2005) determined a spectral classification of O5-6V for the central ionizing star of RCW 121. This spectral type together with JHK_s photometry from 2MASS allow us to calculate a new, independent value for the distance to RCW 121. Assuming intrinsic colours and absolute magnitudes from Martins & Plez (2006), we determined a spectroscopic distance to this star, and thus to the H II region, of 2.0 kpc with an extinction of $A_V = 6.7$. The uncertainties attached to this value come from those in the absolute calibration of the luminosities and colours of the O stars (for a discussion, see Hanson 2003). It is important to note that the above distance is consistent with the near-kinematic values determined from radial velocities of the ionized hydrogen line and of its associated maser source, $d = 1.9$–2.6 kpc (Walsh et al. 1997; Sewilo et al. 2004), respectively. This implies that the region suffers no large velocity deviations from the galactic circular orbit. Thus, a distance of 2.0 kpc to this region can be safely assumed.

At this distance, the projected mean radius of the H II is $R_{\rm H\,II} = 0.4$ pc and its age is, at most, around a few million years (cf. Dyson & Williams 1997). The morphology of practically all the arc-like structures and filaments is clearly defined by the Br γ (2.17 μm) emission (blue contours in Fig. 6), which is very similar to that seen in the J, H (and naturally K_s) images, indicating that scattering dust

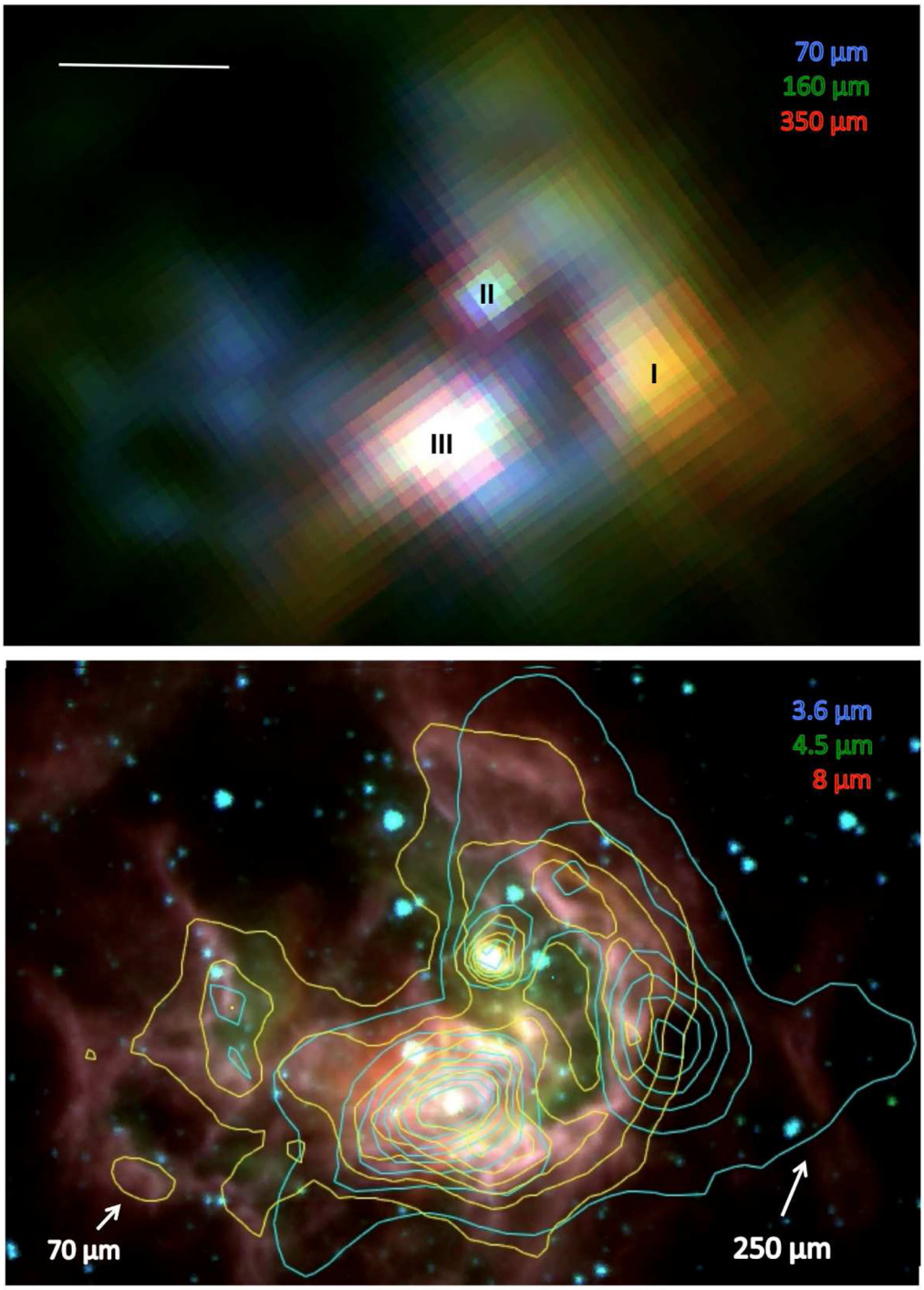

Figure 5. Upper panel: *Herschel* three-colour image constructed from the 70 μm (blue), 160 μm (green) and 350 μm (red) images. The three principal emission peaks, corresponding to dense molecular cores, each heated by an embedded protostar, are labelled I, II and III. Lower panel: *IRAC* three-colour image constructed from 3.6 μm (blue), 4.5 μm (green) and 8 μm (red) images. The superimposed contours correspond to 70 μm (yellow) and 250 μm (cyan) emission as mapped by *Herschel*. All intensity scales are linear. The centre of both panels is at $\alpha(2000) = 17^{\rm h}18^{\rm m}23\overset{\rm s}{.}9$, $\delta(2000) = -39^{\circ}18'46''$. The bar length corresponds to 52 arcsec, or 0.5 pc. North is at the top and east to the left.

particles (that dominate the diffuse near-IR continuum emission) are well mixed with the ionized gas. The compressed layer just outside the expanding ionization front, the PDR, is very well delineated by the emission of polycyclic aromatic hydrocarbons (PAHs) that dominates in the 3.6, 5.8 and 8 μm *Spitzer*/IRAC bands, giving a pinkish colour in the three-colour image in the lower panel of Fig. 5. The 8 μm yellow contours in Fig. 6 also illustrate the spatial distribution of the PAH-dominated emission. This shell is particularly well defined on the western edge of RCW 121. Interestingly, the PACS 70 μm diffuse emission (grey-scale in Fig. 6), follows very closely that of the PAHs (i.e. at 8 μm), and is displaced from the cooler dust thermal emission mapped at longer wavelengths

Table 4. Positions and flux densities of three *Herschel* sources detected in RCW 121.

Source	α(2000) (^{h} ^{m} ^{s})	δ(2000) ($^{\circ}$ $'$ $''$)	F[70] (Jy)	F[160] (Jy)	F[250] (Jy)	F[350] (Jy)	F[500] (Jy)
IRAS 17149-I	17 18 18.9	−39 19 04	–	422.43 (52.15)	333.11 (17.35)	174.91 (9.45)	85.14 (5.01)
IRAS 17149-II	17 18 23.4	−39 18 42	179.19 (12.44)	155.12 (13.85)	94.41 (8.82)	54.19 (6.77)	52.54 (6.18)
IRAS 17149-III	17 18 24.4	−39 19 25	454.50 (12.95)	753.38 (42.32)	526.17 (24.25	221.15 (10.10)	94.20 (5.17)

Table 5. Coordinates and aperture photometry of sources identified on PANIC and IRAC images.[a]

α(2000) (^{h} ^{m} ^{s})	δ(2000) ($^{\circ}$ $'$ $''$)	J (mag)	H (mag)	K_s (mag)	[3.6] (mag)	[4.5] (mag)	Remarks[b]
17 18 20.55	−39 18 12.5	11.92 0.02	11.68 0.02	11.60 0.02	11.55 0.06	11.42 0.07	o, fg
17 18 21.10	−39 18 36.1	–	18.6 0.4	14.5 0.2	12.9 0.3	–	i, nb
17 18 21.19	−39 18 39.2	13.53 0.10	12.39 0.1	11.62 0.05	10.75 0.04	10.89 0.05	i
17 18 21.48	−39 19 13.9	12.75 0.04	11.75 0.04	10.92 0.10	10.28 0.03	9.91 0.04	i
17 18 21.55	−39 18 31.4	14.89 0.07	12.54 0.04	11.44 0.04	10.13 0.08	10.25 0.08	i
17 18 21.69	−39 19 22.1	16.48 0.01	13.58 0.01	11.89 0.01	11.14 0.06	10.46 0.07	i
17 18 21.93	−39 18 32.8	–	17.8 0.2	15.0 0.1	12.9 0.3	–	i, nb
17 18 22.06	−39 19 11.3	17.21 0.02	14.48 0.01	12.94 0.01	11.72 0.25	11.79 0.32	i
17 18 22.21	−39 18 42.2	11.36 0.02	10.04 0.02	8.96 0.02	8.03 0.01	7.43 0.01	i
17 18 22.35	−39 18 21.0	12.78 0.03	11.71 0.05	11.25 0.03	10.65 0.16	11.20 0.22	i
17 18 22.85	−39 18 22.5	14.37 0.08	12.09 0.04	10.09 0.03	8.36 0.01	8.05 0.01	i
17 18 23.29	−39 19 07.8	12.99 0.04	11.91 0.04	11.13 0.06	10.09 0.13	9.71 0.07	i
17 18 23.29	−39 18 27.0	12.91 0.03	12.43 0.03	12.11 0.06	10.64 0.07	10.73 0.11	i
17 18 23.32	−39 18 56.1	12.94 0.05	12.42 0.05	11.86 0.05	11.38 0.07	10.52 0.08	i
17 18 23.41	−39 18 31.3	–	18.4 0.3	15.1 0.1	12.9 0.3	–	i, nb
17 18 23.47	−39 18 40.5	–	18.00 0.08	14.71 0.04	7.77 0.02	6.29 0.01	i, lx, II[c]
17 18 23.79	−39 19 04.3	12.80 0.04	12.18 0.05	11.66 0.06	9.87 0.12	9.88 0.10	i
17 18 24.00	−39 19 15.3	19.43 0.09	17.80 0.05	15.69 0.05	12.9 0.3	–	nb, i
17 18 24.40	−39 18 09.8	16.21 0.01	13.94 0.01	12.75 0.01	11.47 0.06	11.66 0.09	i
17 18 24.40	−39 19 24.6	17.82 0.05	15.53 0.03	12.80 0.01	8.00 0.03	7.47 0.01	i, lx, III[c]
17 18 24.47	−39 18 40.8	17.63 0.04	15.28 0.01	14.02 0.01	11.60 0.11	11.72 0.24	i, db
17 18 24.64	−39 18 41.5	12.65 0.03	12.00 0.05	11.67 0.04	11.29 0.07	10.71 0.08	i
17 18 24.66	−39 18 48.8	–	17.9 0.2	15.1 0.1	13.0 0.3	–	i
17 18 25.11	−39 18 46.4	14.77 0.02	12.49 0.03	11.36 0.02	10.72 0.06	10.98 0.05	i
17 18 25.25	−39 18 37.0	13.51 0.10	12.71 0.03	12.33 0.03	11.60 0.05	11.43 0.09	i
17 18 25.45	−39 19 08.6	8.65 0.02	8.21 0.02	7.93 0.02	7.79 0.01	7.63 0.01	i, C[c]
17 18 25.28	−39 18 24.8	12.82 0.11	11.37 0.04	10.42 0.03	9.64 0.01	9.79 0.02	i
17 18 25.68	−39 18 26.6	11.79 0.02	9.62 0.03	8.61 0.03	7.90 0.01	8.05 0.01	i
17 18 25.94	−39 18 00.9	7.71 0.02	7.19 0.03	7.02 0.02	7.11 0.01	6.99 0.01	o, fg
17 18 26.73	−39 19 34.2	17.57 0.01	15.53 0.01	14.06 0.01	12.63 0.42	11.31 0.10	i
17 18 27.01	−39 19 04.0	17.77 0.02	15.59 0.01	14.02 0.01	12.36 0.12	11.56 0.09	i
17 18 27.12	−39 19 42.6	18.16 0.02	16.09 0.01	14.62 0.02	11.74 0.18	11.42 0.13	o, lx
17 18 27.84	−39 17 58.2	15.30 0.02	13.17 0.02	12.23 0.03	11.36 0.03	11.38 0.04	o
17 18 28.15	−39 19 24.6	15.08 0.01	13.84 0.02	13.22 0.03	12.31 0.18	11.93 0.19	o
17 18 28.30	−39 19 50.0	14.97 0.01	13.74 0.02	13.04 0.03	10.96 0.03	10.35 0.03	o, lx
17 18 28.72	−39 19 15.6	11.23 0.02	11.00 0.03	10.85 0.04	11.05 0.07	11.13 0.08	o, fg
17 18 28.84	−39 19 21.3	16.88 0.09	13.57 0.09	12.68 0.09	10.34 0.18	10.29 0.14	o, lx

[a]Sources with $K < 12.5$ are from 2MASS.
[b]i = in A(in); o = in A(out); x = moderate 3.6 μm excess; lx = large 3.6 μm excess; db = double; nb = nebulous; fg = foreground; II,III = *Herschel* sources; C = central ionizing star.
[c]*IRAC* 5.8 μm magnitude(error) of II: 4.74(0.09); III: 6.16(0.08); C: 7.56(0.21).

(160–500 μm). Fig. 6 also displays the morphology of the 250 μm emission.

The ionized gas emission (Br γ) line is stronger along two distinct arcs. The longest and widest one is located to the south and west of the central ionizing star. This is concave and seems to delineate a section of an expanding ionized gas shell. It appears bright in Br γ, probably because along this arc the ionized gas density is enhanced by higher ambient ram pressure in that direction. In fact, the ionization front seems to have travelled further away from the central ionizing star in most other directions, as seen, for example, by fainter Brackett line emission to the west end of the image. The most conspicuous hydrogen line emission feature is a convex bright arc some 30 arcsec to the north-west of the central ionizing star. This clearly represents a curved ionization front that has encountered a nearly round obstacle that inhibits its radial expansion. The obstacle is a very dense molecular core of approximate diameter 0.13 pc (13 arcsec) and that is characterized by having at its centre the far-IR and millimetre source that we have labelled II in Figs 5 and 6

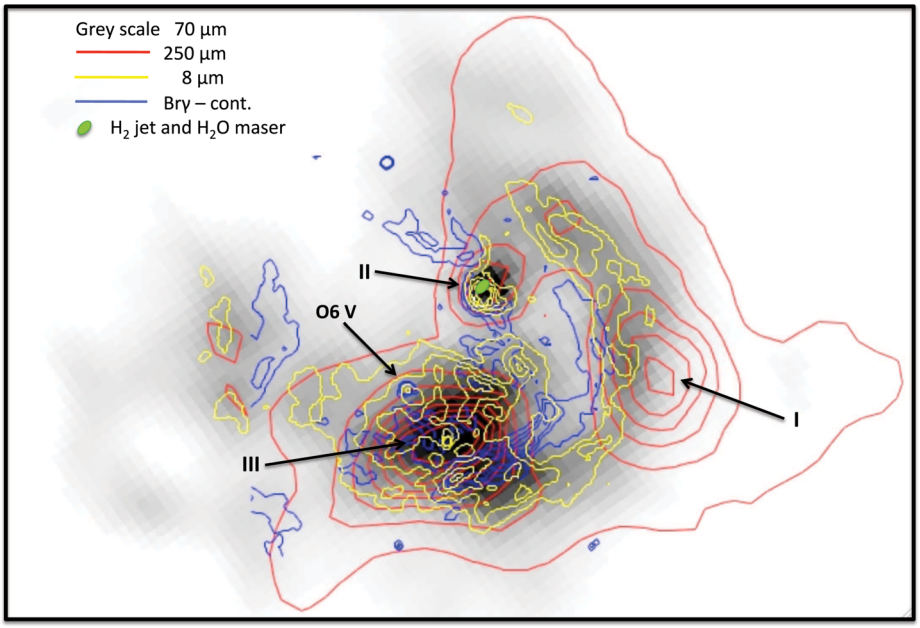

Figure 6. 275 × 180 arcsec^2 PACS 70 μm grey-scale image of the RCW 121 with superimposed contours of the emission at 250 μm (SPIRE), 8 μm (IRAC) and Br γ–continuum (PANIC). Labels I, II and III mark the three dense cores and the label O6V, the central ionizing star. The centre and scale are as in Fig. 5. North is to the top, east to the left.

and that is coincident with a compact near-IR source with an H_2 jet emanating from it (Section 5.2).

4 THE NEAR-INFRARED CLUSTER

The basic properties of the bright population of the young near-IR cluster associated with RCW 121 (Dutra et al. 2003) have been determined by Roman-Lopes & Abraham (2006), though this study was limited by low spatial resolution (∼2 arcsec) and shallow images. The present J, H and K_s deep PANIC images, with subarcsecond resolution, are used for refining the properties of this cluster. The first parameters that we address are the extent of the cluster and the precise location of its centre, assuming a spherical morphology. To determine these, we performed 2.2 μm source counts in concentric rings with 2 arcsec steps in radius, shifting the centre of the rings iteratively until the richest, steepest and smoothest profile was obtained. This occur for a centre at $\alpha(2000) = 17^h18^m24\overset{s}{.}52$, $\delta(2000) = -39°18'56\overset{''}{.}0$. The radius for which the projected source density reaches a level 5 per cent above the mean measured value for the outer radii (assumed to represent the field) was defined to indicate the boundaries of the cluster. This turns out to be $r = 46$ arcsec. Only sources measured with photometric uncertainties lower than 9 per cent were considered for this process in order to avoid possible spurious sources. It is important to note that this restriction was consistently applied in all filters throughout the whole of this photometric analysis. Fig. 7 presents the spatial distribution of all the sources, irrespective of their brightness, with the circle drawn indicating the cluster boundaries, while Fig. 8 shows the observed projected source density profile. The area of the circle defining the cluster boundaries is 1.847 arcmin^2, named A(in) hereafter, while the entire field covered by our three (JHK_s) frames is 4.203 arcmin^2. Thus, the observed area outside the cluster limits amounts to A(out) = 2.356 arcmin^2 and A(in)/A(out) = 0.784.

Fig. 9 shows the $J - H$ versus $H - K_s$ diagram of all sources measured in these three filters in the total field observed and with

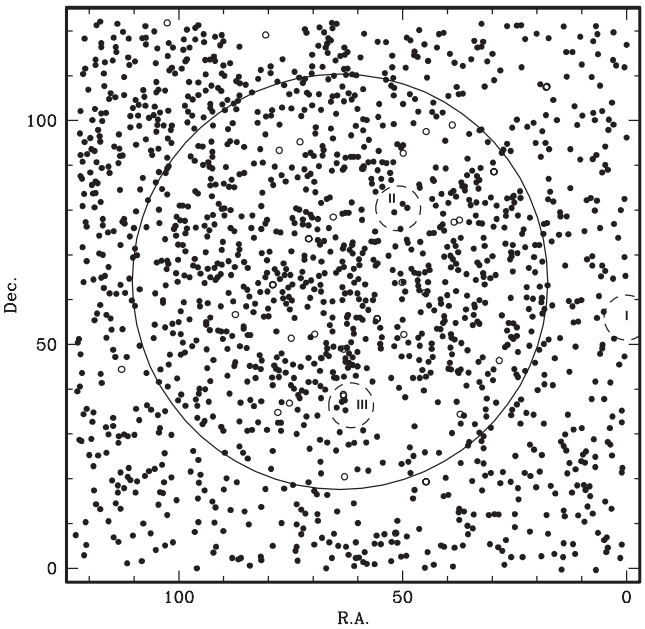

Figure 7. Diagram showing the location of all sources measured on the HK_s PANIC images with uncertainties ≤0.09 (filled points). For sources brighter than $K_s < 12.5$ (open points), the photometry was taken from 2MASS. The large continuous line circle of radius 46 arcsec marks the boundaries of the near-IR cluster (see text). The dashed line smaller circles marks the position of the *Herschel* sources (cores) I, II and III.

uncertainties ≤0.09. In the left-hand panel, we plot the 579 sources located within A(in), while in the right-hand panel, we plot the remaining 423 sources which lie in A(out). Assuming that the source population in A(out) is representative of the local field, we expect 332 (423 × 0.784) field stars to be present in A(in). This means that, statistically, our sample of sources measured in JHK_s within $r < 46$ arcsec contains an excess of about 247 stars, most probably

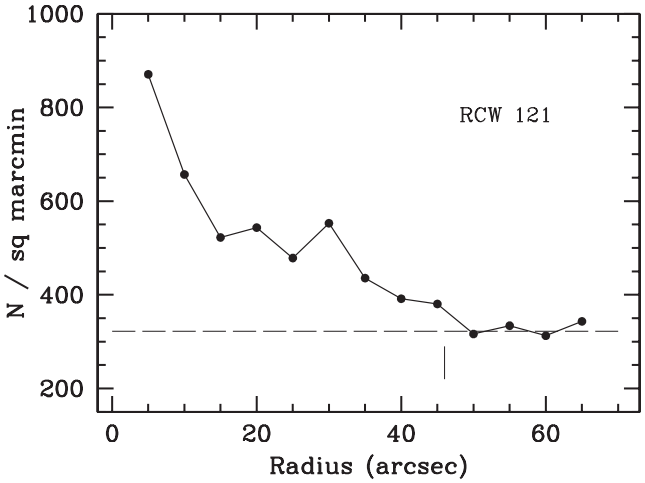

Figure 8. Radial plots of projected source number density determined by source counts in concentring rings on the K_s image. The centre was determined for the steepest and smoothest function, which is $\alpha(2000) = 17^h18^m24^s.52$, $\delta(2000) = -39°18'56''.0$. The dashed line is the assumed field-star density in this direction. The small vertical line shows the assumed radius of the cluster, 46 arcsec.

being cluster members. Defining a star to have near-IR excess (presumably due to the presence of a disc) when its $H - K_s$ index is 0.3 higher than the corresponding value for a stellar photosphere with the same $(J - H)$ index and standard extinction (Rieke & Lebofsky 1985), we find 77 sources (13 per cent) in A(in) with near-IR excess emission. On the other hand, in A(out), that we assume to be representative of the field, only three per cent of the sources are found to have near-IR excess. This implies that 24 per cent of the 247 likely cluster members with measured JHK_s appears to have discs.

It is well known that the analysis of the colour–magnitude diagrams is a most helpful tool to investigate the properties of the stellar population of clusters, and also provide ways to determine some of their physical parameters. Fig. 10 displays the K_s versus $H - K_s$ plots for the RCW 121 region. The left-hand panel includes sources inside A(in), and those in A(out) are plotted in the right-hand panel. In both panels, the nearly vertical continuous lines represent the zero-age main-sequence (ZAMS) at a distance $d = 2.0$ kpc and reddened by $A_V = 5.5$, which are the values determined for the H II region and its central ionizing star (Section 3).

The differences between both diagrams are striking and from these, we infer the following conclusions.

(1) Following the same statistical argument as for the sources with JHK_s photometry, we derive the expected number of cluster members (within A(in)) measured in H and K_s to be 264 (some 10 per cent more than those with JHK_s).

(2) A significant fraction (32 per cent) of field stars, i.e. those in A(out), in the K_s versus $H - K_s$ diagram (right-hand panel of Fig. 10) appear to the left of the ZAMS for the distance of the H II region, meaning that their reddening (i.e. $E(H - K_s)$) is lower than for the nebula and are, thus, in the foreground. Those to the right of the ZAMS (38 per cent) are more highly reddened, and mostly located in the background, while a fraction of them may be physically associated with the RCW 121 complex.

(3) In contrast, the population of HK_s-measured sources inside A(in) shows very different proportion of foreground sources, only 15 per cent. This imply that 85 per cent have larger $E(H - K_s)$ indices than the ZAMS, due to higher extinction than the H II region and/or IR-excesses. Again, subtracting the expected number of field

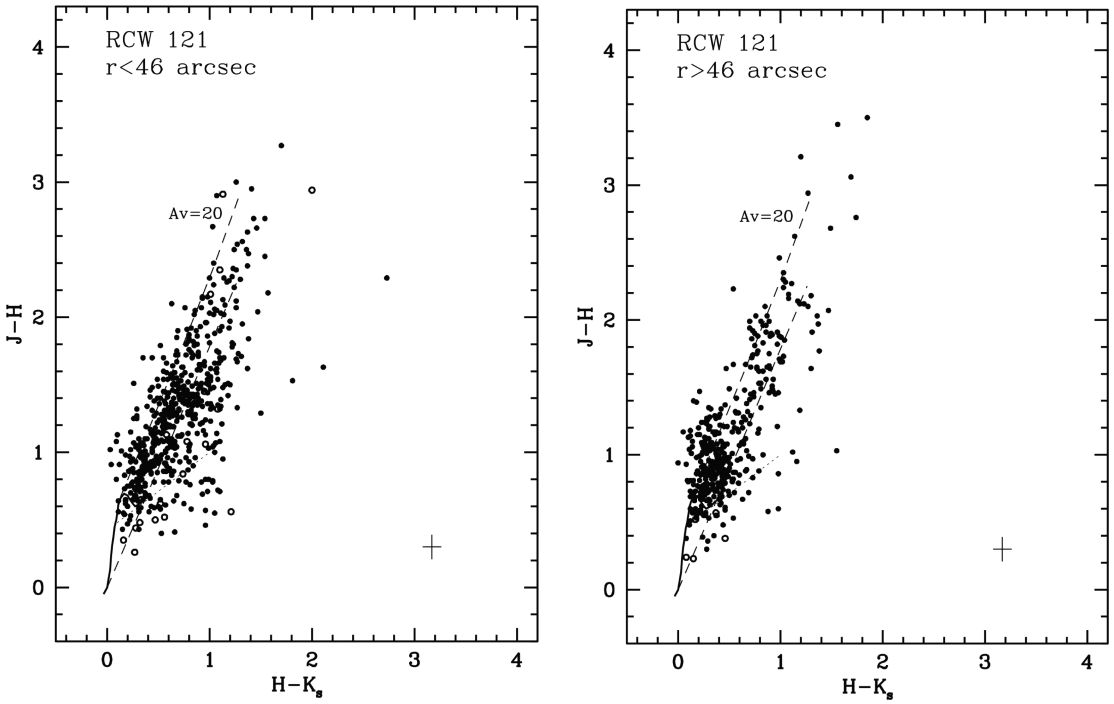

Figure 9. $J - H$ versus $H - K_s$ diagram of all sources measured in JHK_s with uncertainties ≤ 0.09 in each filter (filled symbols). Photometry of sources that saturate are taken from the 2MASS catalogue (open symbols). The left-hand panel is for sources inside the circle of radius $r = 46$ arcsec, and the right-hand panel for sources outside. The solid lines mark the loci of the main sequence (Koornneef 1983), the dashed lines delineate the reddening band for all main-sequence star and giant stars (Rieke & Lebofsky 1985). The small cross near the lower right-hand corner shows the maximum formal error for each measurement.

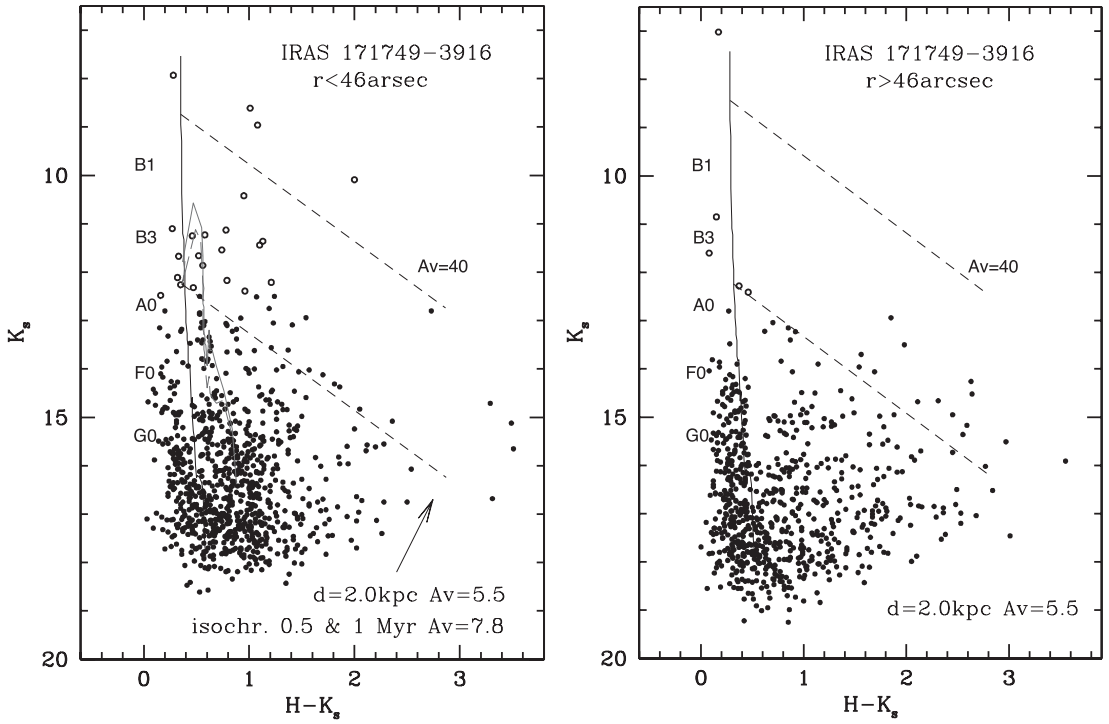

Figure 10. K_s versus $H - K_s$ diagram of sources measured with PANIC in H and K_s with uncertainties $\leq$0.09 in each filter (filled circles). Photometry of sources that saturate are taken from the 2MASS catalogue (open circles). The left-hand panel is for sources inside the $r = 46$ arcsec circle and the right-hand panel plots the sources outside that circle. For reference, the almost vertical solid lines delineate the ZAMS for $d = 2.0$ kpc and $A_V = 5.5$. The dashed lines are the reddening vectors of length $A_V = 40$ for A0 and B1 ZAMS stars. In the left-hand panel, the coloured lines represent the 0.5 Myr (red) and 1 Myr (blue) isochrones (Siess et al. 2000) for the same distance and $A_V = 7.8$ and the arrow represents the average slope of the near-IR emission excess caused by discs around YSOs, as determined by López-Chico & Salas (2007).

background sources, we compute some 320 sources in *A*(in) likely to be associated with the cluster.

(4) On close inspection of the left-hand panel of Fig. 10, it is clear that a large number of these stars, presumably representative of the cluster population, lies to the right and along a line nearly parallel to the ZAMS. As shown in this diagram, reasonable fits of PMS isochrones (from Siess, Dufour & Forestini 2000) to this population are obtained for $A_V = 7.8$ and ages between 5×10^5 and 10^6 yr for an imposed distance of 2.0 kpc. It is, then, natural to assign such mean extinction and an age in this range for the IR cluster inside RCW 121.

(5) As expected for such a young cluster, a relatively large fraction of sources in it exhibit large near-IR excesses, probably due to the presence of discs. In fact, we derived this fraction to be 25 per cent.

(6) We also note that a small number of bright near-IR sources with large K_s-band excesses are located just outside the derived cluster limits. These appear to be associated with the outer layers of the H II region, and may be massive run-away members of the cluster which originally were part of close binaries in the nucleus of the protocluster, and that were dynamically disrupted at a very early stage of its evolution.

Finally, comparing our deep near-IR PANIC frames with the much shallower IRAC images, we find that only 37 near-IR sources had counterparts on the 3.6 and 4.5 μm. These are plotted in the $H - K_s$ versus $K_s - [3.6]$ diagram shown in Fig. 11. The fraction of sources in this sample that shows significant (or large) excesses at 3.6 μm is 52 per cent. 20 per cent of these are located outside the cluster area, and they show with similar statistics. Nevertheless, we

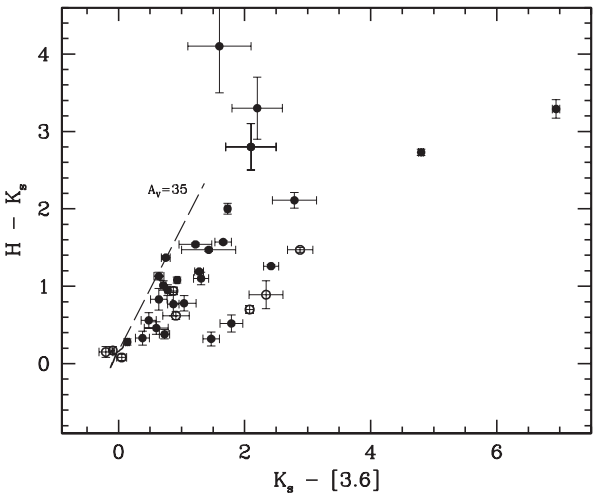

Figure 11. $H - K_s$ versus $K_s - [3.6]$ for all unresolved sources measured on the IRAC 3.6 μm and the H and K_s images. Open circles represent sources outside $r = 46$ arcsec and filled circles, sources inside that radius. The solid line close to the origin represents the locus of the main sequence (Koornneef 1983) and the dashed line represents the reddening vector of length $A_V = 35$ (Tapia 1981).

caution that the statistical analyses from this sample are unreliable, because of the intrinsic bias towards mid-IR bright (and very red) sources at locating the IRAC counterparts.

As will be argued in the following sections, the youngest protostellar objects, with the highest near-IR excesses and also bright

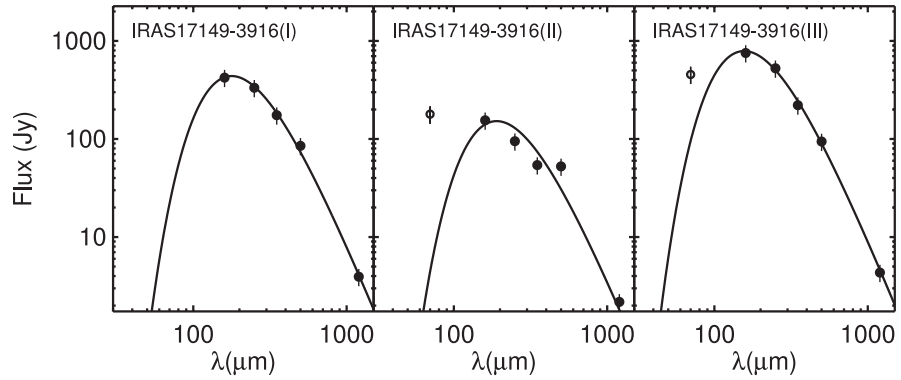

Figure 12. Far-IR and millimetre SEDs of the three cores detected with *Herschel*. The 70 μm measurements (open circles) were not considered for the modified blackbody fit (Section 5).

in the far- and mid-IR, probably belong to a newer generation of stars being formed as a result of the expansion of the developed H II region, interacting with dense clumps in its periphery.

5 MASSIVE DENSE CORES

The three brightest *Herschel* far-IR sources that we detect (named I, II and III) are located at the same positions (within the uncertainties) as three of the dense clumps found at millimetre wavelengths by Beltrán et al. (2006).[3] Their fluxes and positions determined from the 160 to 350 μm frames, are indicated in Table 4. These warm, dense, clumps/far-IR sources are indicative of cores where active star formation has recently (or actively) taken place. This process appears to have been triggered by a PDR created by the expansion of the H II region interacting with material in its vicinity. Hereafter, these far-IR sources are also referred to as cores. Core I is located immediately outside the projected compressed layer ahead of the ionization front to the west, cores II and III are seen, in projection, inside the H II region, but as we will argue later, these may be located in the backside edge of the quasi-spherical H II region.

Using the measured *Herschel* fluxes (Table 4) and those at 1.2 mm (Beltrán et al. 2006), we derived the SEDs for these three most massive clumps. Following the approach generally adopted in the recent literature (Elia et al. 2010; Giannini, Elia & Lorenzett 2012), a single-temperature modified blackbody has been fitted to the far-IR section of the SEDs to derive the mass and temperature of the envelope:

$$F_\nu = \frac{Mk_0}{d^2}\left(\frac{\nu}{\nu_0}\right)^\beta B_\nu(T), \quad (1)$$

where M, d and T are the mass, the distance and the temperature of the envelope, respectively, $k_0 = 0.1$ cm^2 g^{-1} at $\nu_0 = 1200$ GHz, which assumes a gas-to-dust ratio of 100. Finally, the dust emissivity exponent β has been kept constant ($\beta = 2$) to reduce the number of free parameters of the fit. For this purpose, only the data for $\lambda > 100$ μm was considered to avoid any contribution of other warmer components associated with the protostellar content of the core. Fig. 12 illustrates the SEDs of the three dense cores. Assuming for IRAS 17149−3916 a distance of 2.0 kpc (Section 3), the derived masses and temperature for the three cores are reported in Table 6.

[3] The far-IR sources I, II and III described in this paper correspond to Beltrán et al.'s (2006; table 2) millimetre clumps 2, 3 and 1, respectively. Clump 4 has no *Herschel* counterpart.

Table 6. Masses and temperatures of the dense cores in IRAS 17149−3916.

Source	M ($M_\odot$)	T_d (K)
IRAS 17149-I	121.8	19.0
IRAS 17149-II	93.0	15.0
IRAS 17149-III	230.1	16.7

Note that the present determination yields masses of the clumps 10–40 per cent lower than those derived by Beltrán et al. (2006).

6 CONDITIONS AROUND THE MASSIVE DENSE CORES

6.1 IRAS 17149−3916-I

This core lies just outside the PDR created by the expansion of the H II region towards the west, as delineated by the PAH emission which is dominant in the IRAC in 3.6, 5.8 and 8 μm bands. It is important to note that this source has no counterpart in any of the IRAC images (i.e. $\lambda = 3.6$–8 μm) covering this far-IR source. Furthermore, at 70 μm the peak emission occurs at $\alpha(2000) = 17^h18^m19\overset{s}{.}8$, $\delta(2000) = -39^\circ19'06''$, more than 12 arcsec away from the unresolved emission peak at longer wavelengths (Table 4), implying that at this wavelength the protostar was undetected directly. Because of this, the fitted parameters of core IRAS 17149-I given in Table 6 seem to be realistic as no warmer components appear to contribute to the SED. Its total luminosity was computed to be $L_{tot} \simeq 2 \times 10^3\ L_\odot$, which corresponds to that of a B3 ZAMS star. This object is at the earliest stage of star formation that can be detected. The location of this core at the border of the projected circular H II region strongly suggests that the vector joining core I with the central ionizing star is almost perpendicular to the line of sight. No IRAC sources are seen in the vicinity (within 12 arcsec) of IRAS 17149-I and a relatively small number of stars were bright enough to be measured on our deep near-IR images. None of these sources show any emission excess at $\lambda > 2$ μm, confirming that they are most probably unrelated to this core.

6.2 IRAS 17149−3916-II

Out of 57 compact near-IR sources detected on our PANIC JHK_s frames within a radius of 15 arcsec of core II, we found 13 objects

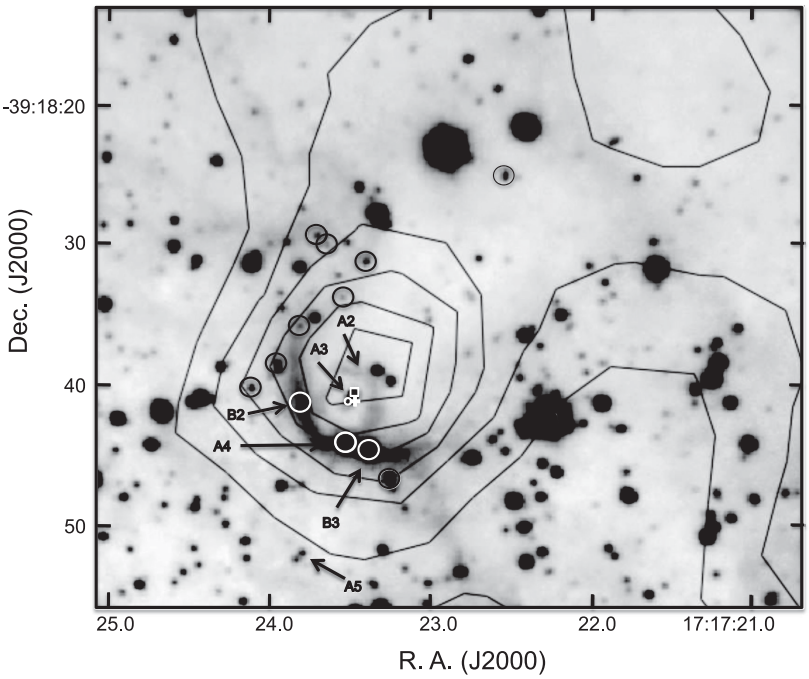

Figure 13. K_s-band image of the core II area showing the distribution of the IR-excess sources (O). The square shows the position of the near- and mid-IR source compact PANIC and IRAC source (see Section 5.2). The plus sign marks the position of the water maser source (Sánchez-Monge et al. 2013), and the small open circle is the H_2 knot. Superimposed are the *Herschel* 160 μm emission contours. The positions of the extracted spectra (Fig. 3 and Table 1) are marked with A2, A3, A4, A5, B2 and B3.

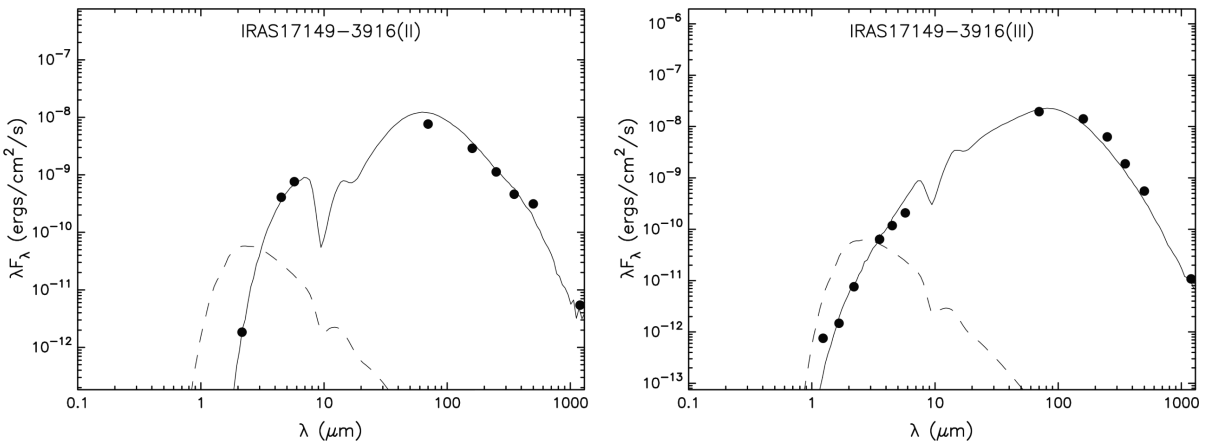

Figure 14. Left-hand panel: SED of source A3 in core II. Right-hand panel: SED of source C3 in core III. The best-fitting model to each of the SEDs derived using Robitaille et al.'s (2007) fitting tool is overplotted as solid line. The fitted parameters of the model for each source are given in Table 7.

that show significant near-IR excess, marked in Fig. 13. Four of these near-IR sources correspond to nebular emission knots, sometimes with a faint point-like source and their K_s-band excesses is probably caused by Br γ (2.17 μm) line emission. With one exception, discussed below, the source population in this small area displays JHK_s characteristics that does not differ from the rest of the near-IR cluster and, thus, is not embedded in core II.

There is one near-IR source of special interest, named A3 (Table 1, Fig. 2), that is too faint to be detectable at J. It coincides with a GLIMPSE unresolved source that is heavily saturated at 8 μm. Given the extremely red colour indices of this source derived from Table 5 ($H - K_s = 3.3$, $K_s - [3.6] = 7.0$), it is natural to associate it with the far-IR *Herschel* source II which lies, within the positional errors, at the same position in the sky. Combining our K_s photometry, the IRAC photometry, the five *Herschel* flux densities of Table 4 and the 1.2 mm measurement by Beltrán et al. (2006), we constructed the SED for this source, illustrated in Fig. 14 (left-hand panel). The SED has been fitted with the infalling envelope+disc+central source radiation transfer model described by Robitaille et al. (2006) by using the fitting tool of Robitaille et al. (2007). The parameters of the model that best fit the SED are listed in Table 7.

This YSO at the centre of the dense core (II; $M_{\rm core} = 93\,{\rm M}_{\odot}$) has a luminosity corresponding to a B2 ZAMS star reddened by more than 50 mag of extinction in V. Our PANIC narrow-band 2.12 μm image shows a bright H_2 jet-like emission knot emanating from the YSO of length $\leq$0.8 arcsec (1600 au) towards the south-east (PA = 135°). Its 1.0–2.5 μm spectrum taken with FIRE (which includes the YSO and jet) is shown in Fig. 3 (IRAS 17149 A3) and the line intensities are reported in Table 2. The 2.0–2.5 μm spectrum

Table 7. Physical parameters of source A3 in core II and source C3 in core III derived from the Robitaille et al. (2007) model.

Parameters	A3 (II)	C3 (III)
Stellar mass ($M_\odot$)	8.26	9.87
Stellar temperature (K)	11 000	9190
Envelope accretion rate ($M_\odot$ yr^{-1})	1.0×10^{-3}	2.7×10^{-3}
Envelope outer radius (au)	1.0×10^{5}	1.0×10^{5}
Envelope cavity angle (°)	31.1	9.2
Disc mass ($M_\odot$)	6.9×10^{-3}	1.7×10^{-3}
Disc outer radius (au)	52.2	73.5
Disc accretion rate ($M_\odot$ yr^{-1})	4.7×10^{-8}	1.3×10^{-8}
A_V	51.4	23.6
D (kpc)	2.0	2.0
L_{bol} ($L_\odot$)	2.6×10^{3}	3.0×10^{3}

is dominated by the series of rotovibrational H_2 lines characteristic of shocked gas, mounted on a weak, very red continuum. The latter likely arises from the YSO and the lines from the jet. In fact, this spectrum is similar to those found in jets associated with YSO and Herbig–Haro objects (e.g. Nisini et al. 2002). Analysis of the relative H_2 line strength is impractical in this case, as there is no way to estimate the value of the extinction towards the jet which, from the lack of detection of any H_2 or [Fe II] shortward of 1.8 μm, is inferred to be very high. The reported position of the H_2O maser (Sánchez-Monge et al. 2013) lies within 0.5 arcsec (0.005 pc) of the jet/YSO system, strongly suggesting a physical association.

Three other near-IR sources with excess at $\lambda > 2$ μm (B3, A4 and B2; Table 1) are located embedded in the arc-shaped Br γ nebulosity (Fig. 13). Their near-IR spectra are dominated by Brackett and Paschen ionic hydrogen emission lines as well as the He I (2.058 μm) lines (Figs 3 and 4 and Tables 2 and 3). In the case of B3, also H_2 and [Fe II] emission is present, with a ratio [Fe II] 1.64 μm/H_2 2.12 μm = 1.03, consistent with the presence of a fast J-shock component (Lorenzetti et al. 2002). Note that the spectrum at A2, which includes a section of a small circular H II nebulosity totally surrounding the YSO (core II), has an emission spectrum similar to that of B3, A4 and B2 with the contribution of a blue continuum of a foreground star in the slit.

The overall morphology of this star-forming subcomplex is consistent with it being located towards the back edge of the H II region. The curved PDR delineating the boundaries of the dense core has its apex pointing towards the central star ionizing RCW 121. The cloudlet produces a 'shadow' extending to the opposite side (i.e. to the north-west), along which no diffuse emission or embedded (or background) near-IR sources are observed. These properties support the suggestion that it was the expansion of the H II region what triggered the star formation in this core.

6.3 IRAS 17149−3916-III

Within a radius of 12 arcsec centred in this *Herschel* source, we find nine unresolved sources that show near-IR excess emission, and in Fig. 15 their positions are indicated over a K_s image. One of these near-IR sources has $J - H$ and $H - K_s$ colour indices that indicate a large K_s-band excess emission, very different from the cluster + field population. This, the reddest and certainly the most interesting YSO in this subregion, named C3, lies at the same position (within the uncertainties) as the peak of the dense *Herschel* core III and an unresolved GLIMPSE source. Its photometry, from Table 5, yields colour indices $H - K = 2.35$ and $K - [3.6] = 3.73$.[4] These colours reflect a value of $A_V = 24$, which is around half (in magnitudes) the extinction towards source A3 in core II. Combining our near-IR observations with *Spitzer*, *Herschel*, and 1.2 mm measurements, we obtained its SED (Fig. 14, right-hand panel). The parameters of the best fit using Robitaille et al.'s (2007) model are listed in Table 7. Its luminosity is similar to that of a B2 ZAMS star.

The IRAS 17149-III core is only some 20 arcsec to the south-west of the central ionizing star of RCW 121. This undoubtedly is a projection effect, as the very high extinction towards this centre of active star formation suggests, it is most probably located at the back edge of the developed H II region. Its projected morphology at several IR wavelengths is somewhat more complex than the other cores in the region as can be seen in Figs 5, 6 and 15. The Br γ emission (represented by blue contours in Fig. 6) around source C3 appears filamentary and knotty, in what seems like a chaotic way. This description also applies to the diffuse emission present on the four IRAC images at 3.6, 4.5, 5.8 and 8 μm, though the detailed morphology changes somewhat in each spectral channel, implying changes in the distribution of the ionized, small PAHs and large grains (Fig. 6). In all *Herschel* images, source III peaks at the position of the IR source C3, and it appears extended and irregular, probably reflecting at these wavelengths a chaotic distribution of the cooler dust around this core. Our near-IR spectrum associated with this source, shown in Fig. 4, displays a very red continuum from the YSO with hydrogen and helium emission lines arising from the associated H II region, very similar to the spectrum B3 described in the previous section.

7 CONCLUSIONS

In the present work we study the massive star formation complex IRAS 17149−3916/RCW 121 in the light of new deep near-IR broad- and narrow-band (JHK_s and Br γ and H_2) imaging and low-resolution spectroscopy from 0.9 to 2.5 μm that were obtained with the Baade/Magellan Telescope at Las Campanas Observatory. We analyse these in conjunction with new 70, 160, 250, 350 and 500 μm images taken with PACS and SPIRE on board *Herschel*, complemented with archive *Spitzer* IRAC (3.6, 4.5, 5.8 and 8 μm) images. With photometric measurements in all these bands, we identified three bright far-IR sources at the centre of dense cores that are located in the outskirts of an expanding H II region, which is powered by a single, central ionizing O5-6V star. The analyses of the 1–1200 μm SEDs of these far-IR sources, named IRAS 17149-I, IRAS 17149-II and IRAS 17149-III, indicate that they are massive YSO with luminosities of early-B ZAMS stars. Core I, undetected at $\lambda < 100$ μm, is at the earliest observable evolutionary stage (the so-called starless phase), while each of the other cores (II and III) are in more advanced evolutionary stages, each with a massive envelope and disc surrounding the recently formed star. We find that the YSO in core II has an H_2-bright jet emanating very close to it with an associated water maser. We confirm the presence of a near-IR stellar cluster of approximately 92 arcsec in diameter. It is composed of at least 264 members, with approximately 25 per cent of these showing excess emission at $\lambda > 2.0$ μm, indicative of the presence of discs. A 10^6-yr isochrone with $A_V = 7.8$ or slightly

[4] Although the IRAC spatial resolution is lower than that of PANIC, close inspection of the relevant images clearly indicates that the flux contribution at $\lambda > 3$ μm of the few faint near-IR sources in the close vicinity (within ∼1.5 arcsec) is negligible.

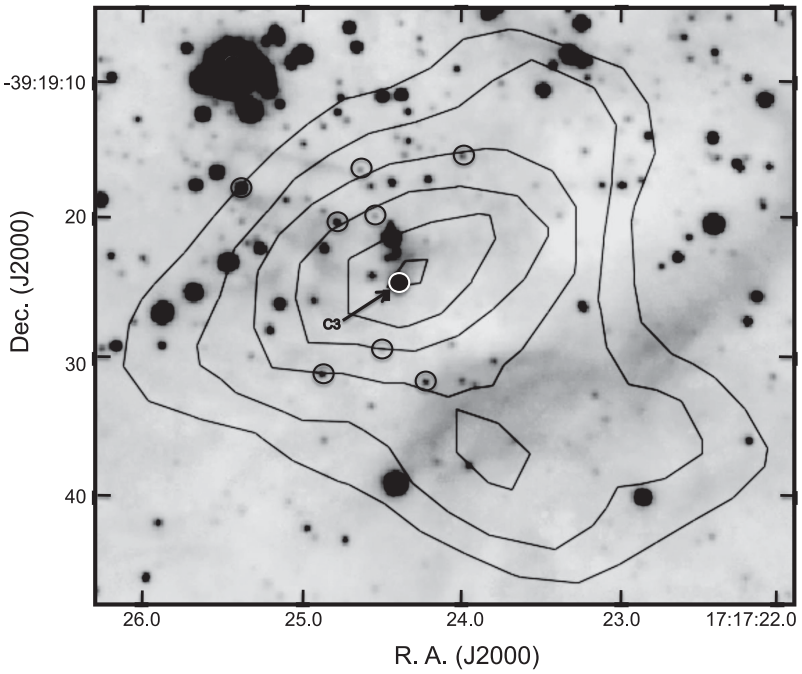

Figure 15. K_s-band image of the area around core III showing the distribution of the IR-excess sources (O). The positions of the spectra observed in this region is marked with C3. Superimposed are the *Herschel* 70 μm emission contours.

younger age fits well the location of a large fraction of likely cluster members in the K_s versus $H - K_s$ diagram.

The presence of three protostellar objects at the borders of a developed H II region associated with a near-IR cluster can be understood in terms of the following simplified scenario: the compressed layer just outside the ionization front created by the expansion of an H II region (Dyson & Williams 1997) is well delineated by the observed emission of polycyclic aromatic hydrocarbons (PAHs) which dominates in the 3.6, 5.8 and 8 μm *Spitzer*/IRAC bands. This dense shell of compressed material interacts mechanically with the neutral external material as it encounters denser, probably pre-existing, molecular condensations, triggering the formation of a new generation of stars that are at present observed as YSOs still embedded in their dense cores. This process is well documented for a number of other massive ionized bubbles that have been observed with *Herschel*, like RCW 120 (Zavagno et al. 2010) and other similar H II regions (e.g. Brand et al. 2011; Anderson et al. 2012).

ACKNOWLEDGEMENTS

MT acknowledges support for this work through PAPIIT-UNAM grants IN100210 and IN101813. This paper makes use of archival data obtained with the *Spitzer Space Telescope*, which is operated by the Jet Propulsion Laboratory, California Institute of Technology (CIT) under National Aeronautics and Space Administration (NASA) contract 1407. This publication also makes use of data products from the Two Micron All Sky Survey (2MASS), which is a joint project of the University of Massachusetts and the Infrared Processing and Analysis Center/California Institute of Technology, funded by the National Aeronautics and Space Administration and the National Science Foundation. We thank our anonymous referee for suggestions that led to a significant improvement in the clarity of this paper.

REFERENCES

Anderson L. D. et al., 2012, A&A, 542, A10
Arnal E. M., Duronea N. V., Testori J. C., 2008, A&A, 486, 807
Beltrán M. T., Brand J., Cesaroni R., Fontani F., Pezzuto S., Testi L., Molinari S., 2006, A&A, 447, 221
Benjamin R. A. et al., 2003, PASP, 115, 953
Bik A., Kaper L., Hanson M. M., Smits M., 2005, A&A, 440, 121
Brand J., Massi F., Zavagno A., Deharveng L., Lefloch B., 2011, A&A, 527, A62
Bronfman L., Nyman L., May J., 1996, A&AS, 115, 81
Carey S. J. et al., 2009, PASP, 121, 76
Churchwell E. et al., 2009, PASP, 121, 213
Dutra C. M., Bica E., Soares J., Barbuy B., 2003, A&A, 400, 533
Dyson J. E., Williams D. A., 1997, The Physics of Interstellar Medium. IoP Publishing, Bristol
Elia D. et al., 2010, A&A, 518, L97
Elmegreen B. G., 1998, in Woodward C. E., Shull J. M., Thronson H. A., eds, ASP Conf. Ser. Vol. 148, Origins. Astron. Soc. Pac., San Francisco, p. 150
Fazio G. et al., 2004, ApJS, 154, 10
Giannini T., Elia D., Lorenzett D., 2012, A&A, 539, A156
Griffin M. J. et al., 2010, A&A, 518, L3
Hanson M. M., 2003, ApJ, 597, 957
Haro G., 1952, Bol. Obser. Tonantzintla Tacubaya, 1, 1
Koornneef J., 1983, A&A, 128, 84
López-Chico T. A., Salas L., 2007, Rev. Mex. Astron. Astrofis., 43, 155
Lorenzetti D., Giannini T., Vitali F., Massi F., Nisini B., 2002, ApJ, 564, 839
Martini P., Persson S. E., Murphy D. C., Birk C., Shectman S. A., Gunnels S. M., Koch E., 2004, Proc. SPIE, 5492, 1653
Martins F., Plez B., 2006, A&A, 457, 637
Molinari S. et al., 2010, A&A, 518, L100
Molinari S., Schisano E., Faustini F., Pestalozzi M., di Giorgio A. M., Liu S., 2011, A&A, 530, A133
Nisini B., Carattio Garatti A., Giannini T., Lorenzetti D., 2002, A&A, 393, 1035

Persson S. E., Murphy D. C., Krzeminski W., Roth M., Rieke M. J., 1998, AJ, 116, 2475
Pilbratt G. L. et al., 2010, A&A, 518, L1
Poglitsch A. et al., 2010, A&A, 518, L2
Rieke G. H., Lebofsky M. J., 1985, ApJ, 288, 618
Robitaille T. P., Whitney B. A., Indebetouw R., Wood K., Denzmore P., 2006, ApJS, 167, 256
Robitaille T. P., Whitney B. A., Indebetouw R., Wood K., 2007, ApJS, 169, 328
Rodgers A. W., Campbell C. T., Whiteoak J. B., 1960, MNRAS, 121, 103
Roman-Lopes A., Abraham Z., 2006, AJ, 131, 951
Sánchez-Monge Á., Beltrán M. T., Cesaroni R., Fontani F., Brand J., Molinari S., Testi L., Burton M., 2013, A&A, 550, A21
Sewilo M., Watson C., Araya E., Churchwell E., Hofner P., Kurtz S., 2004, ApJS, 154, 553
Siess L., Dufour E., Forestini M., 2000, A&A, 358, 599
Simcoe R. A. et al., 2013, PASP, 125, 270
Skrutskie M. F. et al., 2006, AJ, 131, 1163
Stetson P. B., 1987, PASP, 99, 191
Tapia M., 1981, MNRAS, 197, 949
Tapia M., Persi P., Bohigas J., Roth M., Gómez M., 2006, MNRAS, 367, 513
Traficante A. et al., 2011, MNRAS, 416, 2932
Walsh A. J., Hyland A. R., Robinson G., Burton M. G., 1997, MNRAS, 291, 261
Walsh A. J., Burton M. G., Hyland A. R., Robinson G., 1998, MNRAS, 301, 640
Werner M. et al., 2004, ApJS, 154, 1
Wright A. E., Griffith M. R., Burke B. E., Ekers R. D., 1994, ApJS, 91, 111
Zavagno A. et al., 2010, A&A, 518, L81

This paper has been typeset from a TEX/LATEX file prepared by the author.